catalysts

MDPI

Article

Vertical Growth of WO_3 Nanosheets on TiO_2 Nanoribbons as 2D/1D Heterojunction Photocatalysts with Improved Photocatalytic Performance under Visible Light

Ling Wang [1], Keyi Xu [1], Hongwang Tang [2] and Lianwen Zhu [2,*]

[1] College of Chemistry and Life Science, Zhejiang Normal University, Jinhua 321004, China
[2] School of Biology and Chemical Engineering, Jiaxing University, Jiaxing 314001, China
* Correspondence: lwzhu@mail.zjxu.edu.cn

Abstract: We report the construction of 2D/1D heterojunction photocatalysts through the hydrothermal growth of WO_3 nanosheets on TiO_2 nanoribbons for the first time. Two-dimensional WO_3 nanosheets were vertically arrayed on the surface of TiO_2 nanoribbons, and the growth density could be simply controlled by adjusting the concentration of the precursors. The construction of WO_3/TiO_2 heterojunctions not only decreases the band gap energy of TiO_2 from 3.12 to 2.30 eV and broadens the photoresponse range from the UV region to the visible light region but also significantly reduces electron–hole pair recombination and enhances photo-generated carrier separation. Consequently, WO_3/TiO_2 heterostructures exhibit improved photocatalytic activity compared to pure WO_3 nanosheets and TiO_2 nanoribbons upon visible light irradiation. WO_3/TiO_2-25 possesses the highest photocatalytic activity and can remove 92.8% of RhB pollutants in 120 min. Both further increase and decrease in the growth density of WO_3 nanosheets result in an obvious reduction in photocatalytic activity. The kinetic studies confirmed that the photocatalytic degradation of RhB follows the kinetics of the pseudo-first-order model. The present study demonstrates that the prepared WO_3/TiO_2 2D/1D heterostructures are promising materials for photocatalytic removal of organic pollutants to produce clean water.

Keywords: WO_3/TiO_2; 2D/1D heterojunction; photocatalytic activity; water purification

Citation: Wang, L.; Xu, K.; Tang, H.; Zhu, L. Vertical Growth of WO_3 Nanosheets on TiO_2 Nanoribbons as 2D/1D Heterojunction Photocatalysts with Improved Photocatalytic Performance under Visible Light. *Catalysts* **2023**, *13*, 556. https://doi.org/10.3390/catal13030556

Academic Editors: Yongming Fu and Qian Zhang

Received: 12 January 2023
Revised: 6 March 2023
Accepted: 7 March 2023
Published: 9 March 2023

1. Introduction

The demand for fresh water increases exponentially with global population growth and industrial development [1–3]. Clean water scarcity is one of the most pressing issues for human beings to confront nowadays, especially in developing countries [4]. According to World Wildlife, two-thirds of the world's population will face water shortages by 2025 [5]. To address this challenge, many advanced technologies have been developed to remove aqueous pollutants for clean water production [6,7], including adsorption [8,9], membrane filtration [10], and semiconductor photocatalytic technology [11]. Among various techniques, semiconductor photocatalysis offers a green and sustainable water purification technology because harmful pollutants can be completely decomposed to CO_2, H_2O, and other small molecules without the involvement of any chemicals [11–14]. Mainly, photocatalysts absorb photons as an energy source to (1) generate electron−hole pairs, (2) separate the photoexcited charges, (3) transfer electron and hole to the photocatalyst's surface, and (4) utilize the active charges on the photocatalyst's surface for catalytic decomposition of pollutants [12–17].

Heterojunction photocatalysts, particularly systems consisting of a low-dimensional 1D and 2D semiconductor, are recognized as prospective building blocks for next-generation advanced photon harvesting and conversion technologies [18,19]. The considerable potential of 1D/2D heterojunctions arises from high charge carrier mobility along the 1D nanostructures and effective charge recombination prevention ability of 2D nanostructures

due to the strong electron confinement effect in atomic-thick layers. Among four different configurations based on interfacial contact, heterojunctions with vertically aligned 2D nanosheets on 1D nanostructures are highly desirable for photocatalytic systems [19]. That is because the vertically aligned 2D nanosheets on 1D nanostructures not only allow maximum exposure of the entire surface, thereby maximally providing the edge active sites, but also create better electronic contacts and optimized electron transport pathways, leading to enhanced photo-generated electron–hole separation efficiency [18,19]. This unique 2D array on 1D structures widely exists in nature, such as leaf array on a tree branch and the bony plates along stegosaur backs, and their advancement in light absorption and conversion have been proven in nature for millions of years.

Since the discovery of the Honda–Fujishima effect in 1972 [20], TiO_2 has been considered to be the most promising photocatalyst because of its high photosensitivity, excellent stability, nontoxic nature, and low cost [13,21,22]. In particular, 1D TiO_2 nanoribbons have received much more attention for advanced photocatalyst design because of the following features [22–24]. First, the well-defined 1D geometry facilitates fast and long-distance electron transport, leading to long-time photocatalytic stability. Second, 1D nanoribbons possess larger specific surface areas than corresponding bulk materials, providing more active catalytic sites. Third, the large length-to-diameter ratio of 1D nanoribbons increases light absorption and scattering, enhancing light use efficiency [19,20]. Beside TiO_2, WO_3 is another extensively investigated photocatalyst driven by its narrow band gap and visible light absorption ability [25–27]. Among various morphologies, 2D WO_3 nanosheets possess an extremely high percentage of exposed surfaces and a strong quantum confinement effect in the thinnest dimension, leading to abundant active sites and enhanced light conversion efficiency, which are highly desirable for high-performance photocatalysts [25–30]. Inspired by the booming progress in 1D TiO_2 nanoribbon and 2D WO_3 nanosheet photocatalysts, the rational design of 2D/1D WO_3/TiO_2 multidimensional heterojunction photocatalysts is expected to integrate the merits of both 1D and 2D nanogeometry and lead to enhanced photocatalytic performance. Particularly, a 2D WO_3 array on a 1D TiO_2 heterojunction is of special interest for highly efficient photocatalyst design. Coupling narrow band gap WO_3 (2.4–2.8 eV) can not only broaden the absorption wavelength of TiO_2 from UV to visible light regions, resulting in the formation of visible light-responded heterojunction photocatalysts, but also effectively suppresses electron−hole pair recombination, thus improving the photocatalytic activity [31]. To date, substantial efforts have been devoted to construct WO_3/TiO_2 heterojunction systems, including WO_3 nanorod/TiO_2 nanofiber composite [32], WO_3 nanoparticle/TiO_2 nanoparticle composite [33,34], heterostructured TiO_2/WO_3 porous microspheres [35,36], a WO_3 nanoparticle/TiO_2 nanotubes system [37–39], heterostructured WO_3/TiO_2 nanosheets [40,41], and WO_3 nanosheet/TiO_2 nanoparticle composite [42]. However, to the best of our knowledge, 2D/1D heterojunction photocatalysts composed of TiO_2 nanoribbons and WO_3 nanosheets have not been reported. Demonstrating the vertical growth of WO_3 nanosheets on TiO_2 nanoribbons for 2D/1D heterojunction photocatalysts is especially challenging.

Herein, we report the vertical growth of WO_3 nanosheets on TiO_2 nanoribbons as 1D/2D heterojunction photocatalysts with improved photocatalytic performance under visible light. The WO_3/TiO_2 heterojunctions were constructed through the introduction of TiO_2 nanoribbons into the hydrothermal growth system of WO_3 nanosheets. The as-obtained WO_3/TiO_2 sample was characterized by using XRD, SEM, TEM, XPS, UV–vis, and PL analysis. WO_3 nanosheets vertically arrayed on the surface of TiO_2 nanoribbons lead to the formation of 1D/2D heterojunctions with maximum exposure of the entire surface, which not only broadens the light adsorption spectrum into the visible region but also inhibits the recombination of photoinduced carriers, resulting in enhanced photocatalytic degradation of aqueous pollutants.

2. Results and Discussion

2.1. XRD Analysis

The hydrothermal growth process is accompanied by an obvious color change in TiO_2 from white to yellow-green (Figure 1a), indicating the successful and uniform growth of WO_3 on TiO_2. In order to confirm WO_3 growth, XRD patterns of the samples before and after hydrothermal reaction were recorded (Figure 1b). Before growth of WO_3 nanosheets, all the diffraction peaks located at 25.3°, 37.8°, 48.0°, 53.9°, 55.0°, 62.1°, 62.7°, and 68.8° can be indexed to anatase TiO_2 (JCPDS file no. 21-1272), which is in good agreement with previous reports [43,44]. After the growth of the WO_3 nanosheets, except for the peaks originating from TiO_2 nanoribbons (marked with red boxes), new peaks (marked with blue circles) centered at 16.5°, 25.6°, 30.5°, 33.4°, 34.1°, 34.8°, 38.9°, 44.1°, 45.9°, 46.3°, 49.6°, 52.6°, 56.2°, 57.2°, 58.4°, 61.2°, 64.3°, and 66.0° were observed, which match well with $WO_3 \bullet H_2O$ (JCPDS file no. 43-0679) [45], indicating the formation of WO_3/TiO_2-25 composites [32–34].

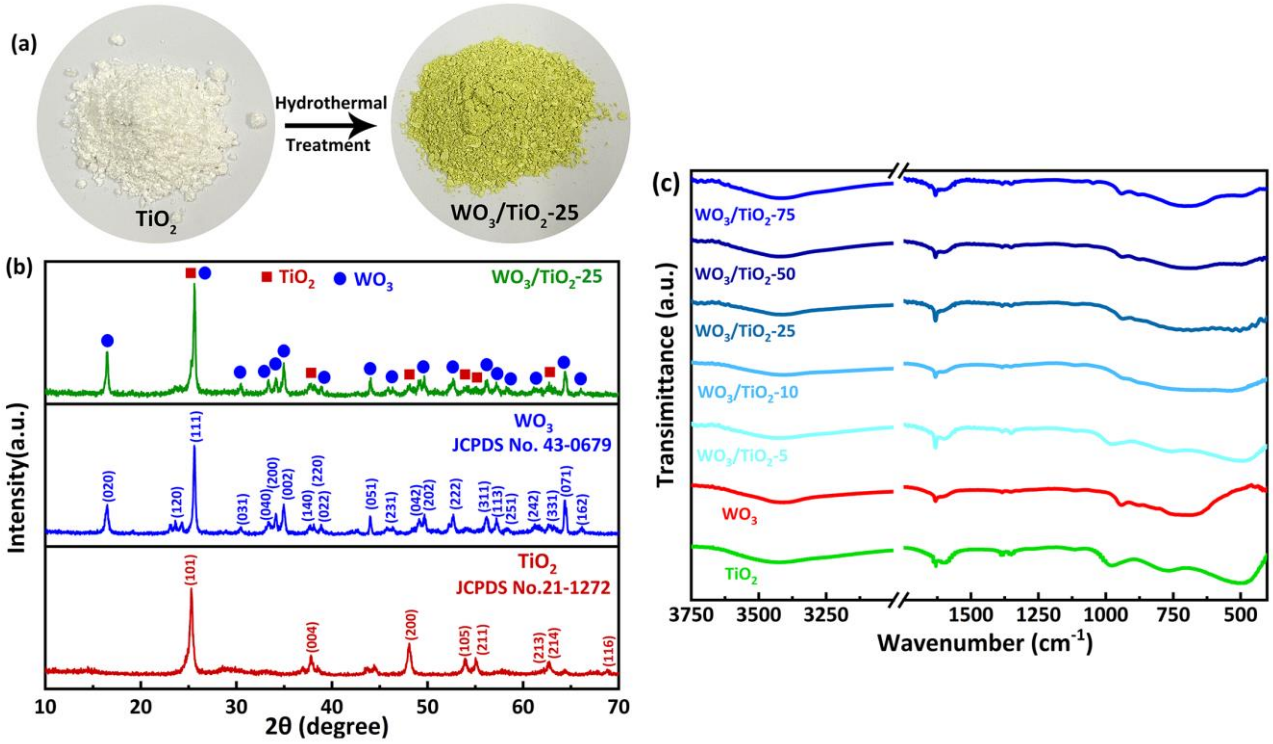

Figure 1. (**a**) Photograph of TiO_2 before and after hydrothermal growth of WO_3. (**b**) XRD patterns of TiO_2, WO_3, and WO_3/TiO_2-25. (**c**) FTIR spectra of TiO_2, WO_3, and WO_3/TiO_2 composites with different ratios.

2.2. FTIR Analysis

In order to further confirm the formation of WO_3/TiO_2 composites, FTIR spectra of all samples have been collected and shown in Figure 1c. For the spectrum of pure TiO_2 nanoribbons (green line), the broad adsorption band centered at 3430 cm^{-1} could be ascribed to the stretching vibrations of the surface hydroxyl groups and molecularly chemisorbed water [46]. The peak at 1630 cm^{-1} results from -OH bending of molecularly physisorbed water [46]. The large absorption in the range 492 cm^{-1} can be attributed to the strong stretching vibrations of the Ti-O bond in TiO_2 nanoribbons [46]. For the spectrum of pure WO_3 nanosheets (red line), the broad adsorption band center at 3410 cm^{-1} is related to the stretch region of the surface hydroxyl groups with hydrogen bonds and crystal water of $WO_3 \bullet H_2O$, while the peak centered at 1633 cm^{-1} is from O–H bending of physisorbed water. The weak band observed around 600–750 cm^{-1} is attributed to the O–W–O stretching

modes of WO_3, and the peak located at 941 cm^{-1} is associated with W=O stretching [46]. For WO_3/TiO_2 composites with different ratios, the broad peak around 3412–3420 cm^{-1} of each sample can be ascribed to the stretching vibrations of -OH groups [46]. These characteristic absorption peaks of WO_3 and TiO_2 located in the range of 400–1000 cm^{-1} are all observed in the spectra of WO_3/TiO_2 composites, indicating the successful combination of WO_3 and TiO_2. From WO_3/TiO_2-5 to WO_3/TiO_2-75, the intensity of peaks from TiO_2 nanoribbons decreases, and the intensity of peaks ascribed to WO_3 nanosheets increases, indicating the increasing growth density of WO_3 nanosheets on TiO_2 nanoribbons, which is in good agreement with the raw material proportioning.

2.3. SEM and TEM Analysis

In order to reveal the configuration of WO_3/TiO_2 heterojunctions, SEM and TEM were applied to observe the pure TiO_2 nanoribbons and the WO_3/TiO_2-25 heterostructure. Before WO_3 growth, pure TiO_2 nanoribbons exhibit typical 1D morphology with a length from several tens to several hundreds of micrometers (Figure 2a). TEM images (Figure 2b–d) of an individual nanoribbon show that the width of the nanoribbons is around 100 nm and the surface of the nanoribbons are flat and clean, which provides comfortable platforms for the nucleation and growth of WO_3 nanosheets. After WO_3 growth, the 1D typical morphology is still maintained, while the surface of the nanoribbons is vertically arrayed with tetragonal nanosheets at a length of 100 nm to 400 nm and thickness of 40 nm (Figure 2e). A similar structure has also been reported in $BiOBr/TiO_2$ systems [43]. A TEM image (Figure 2f) of a single heterostructured nanoribbon demonstrates that 2D nanosheets were grown on both sides of the nanoribbons, leading to the formation of vertically aligned 2D/1D heterostructures with maximum exposure of junctions and the entire surface. High-magnification TEM images (Figure 2g,h) show very clear crystalline planes with a d-spacing of 0.347 nm, which closely matched the inter-planar spacing of the (111) facets of WO_3 [45], further confirming the successful formation of WO_3/TiO_2 heterojunctions. Figure 2i–l show HAADF-STEM-EDS mapping images of a typical nanoribbon arrayed with sheet structures. Ti and O elements can be found in the nanoribbons, while W and O elements existed in the nanosheets, which directly proves that the nanoribbons were TiO_2 and the nanosheets arrayed on nanoribbons were WO_3. These results visually verified that the flat TiO_2 nanoribbons served as the backbones and the WO_3 nanosheets with a tetragonal profile were arrayed on them, leading to the formation of typical vertically aligned 2D on 1D heterostructures. This unique 2D array on 1D structures widely exist in nature and their advancement in light absorption and conversion have been proved in nature for millions of years. For example, trees adopt a leaf array on branch structures to obtain enough access to maximum light. Stegosaurs possessed bony plates along their backs to absorb more heat from the sun to warm their blood on cool days. Therefore, 2D WO_3/1D TiO_2 heterostructures are anticipated to be highly desired for the design of advanced photocatalytic systems.

The growth density of WO_3 nanosheets can be regulated simply via control over the precursor concentration. When the concentration of the precursors was decreased to 5 mM, few nanosheets could be observed on the surfaces of the nanoribbons (Figure S1a). At 10 mM precursor concentration, only a small amount of nanoribbons was decorated with WO_3 nanosheets (Figure S1b). On increasing the precursor concentration to 50 mM, a much higher density of nanosheets could be grown on the nanoribbon backbones, and some isolate nanosheets (Figure S1c) were found between nanoribbons. Further increasing the precursor concentration to 75 mM would lead to a large amount of free nanosheets (Figure S1d), indicating the formation of the mixture of WO_3/TiO_2 heterojunctions and WO_3 nanosheets (Figure S2).

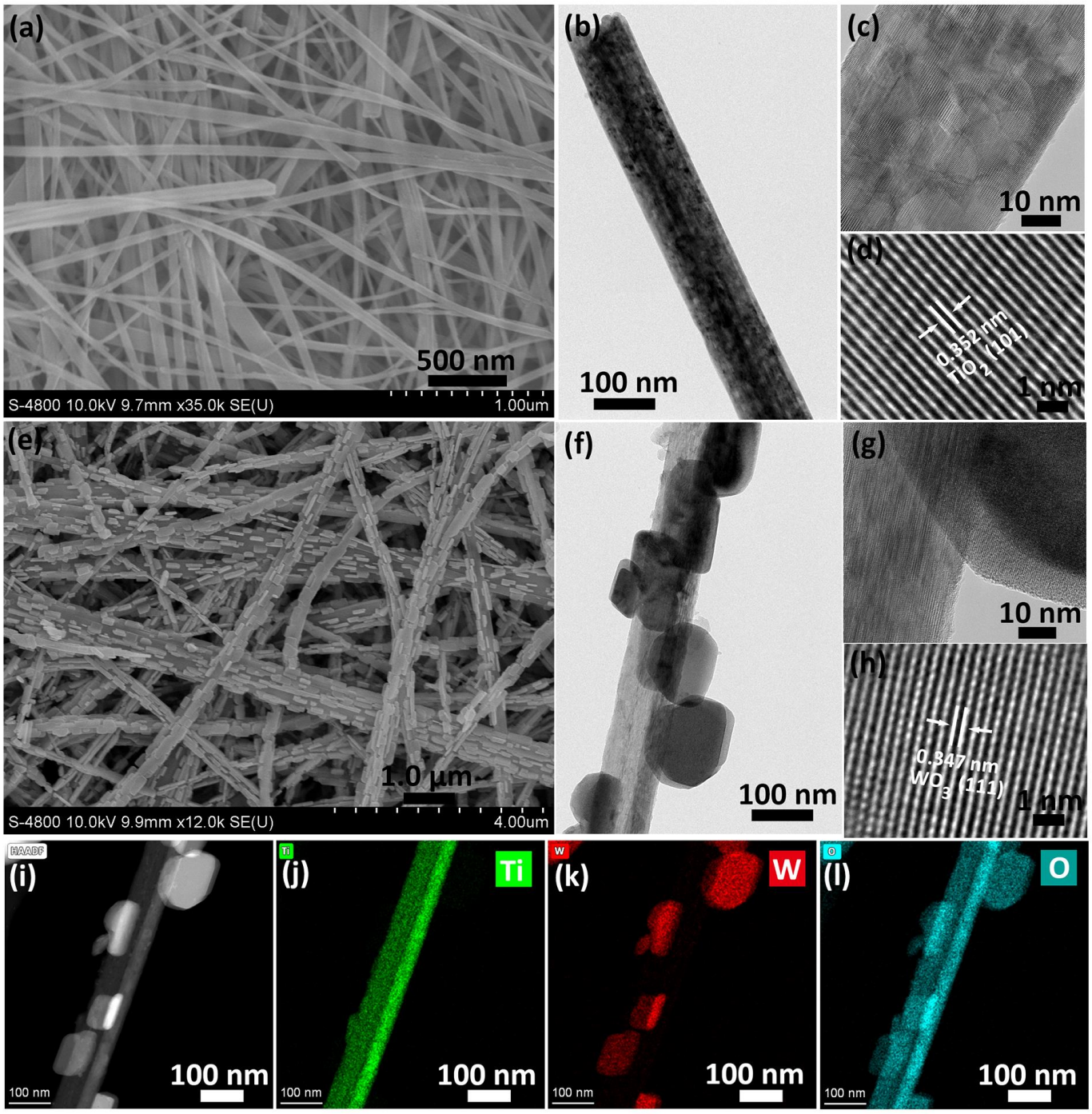

Figure 2. (**a**) SEM image of TiO_2 nanoribbons. (**b**–**d**) TEM images of TiO_2 nanoribbons. (**e**) SEM image of WO_3/TiO_2-25 heterostructure. (**f**–**h**) TEM images of WO_3/TiO_2-25 heterostructure. (**i**–**l**) HAADF-STEM micrograph of WO_3/TiO_2-25 heterostructure and the corresponding EDS mapping of Ti, W, and O.

2.4. XPS Analysis

The element composition and valence of WO_3/TiO_2-25 composite were analyzed by X-ray photoelectron spectroscopy (XPS). Figure 3a shows the Ti 2p spectra of pure TiO_2 nanoribbons and WO_3/TiO_2-25 heterojunctions. The pure TiO_2 nanoribbons exhibit two XPS peaks at 458.6 eV and 464.3 eV, which correspond to Ti $2p_{1/2}$ and Ti $2p_{3/2}$, respectively. The energy gap between Ti $2p_{1/2}$ and Ti $2p_{3/2}$ peaks is 5.7 eV, revealing the oxidation state of Ti in TiO_2 nanoribbons is +4 [36,47], which is also consistent with the XRD

result. After the growth of WO_3 nanosheets on TiO_2, both the Ti $2p_{1/2}$ and Ti $2p_{3/2}$ peaks exhibit obvious red shifts from 458.6 to 459.1 eV and from 464.3 to 464.8 eV, respectively. This result suggests the conversion of Ti-O-Ti bonds to Ti-O-W bonds, which confirms the strong interaction between WO_3 and TiO_2 in the WO_3/TiO_2-25 heterojunctions [34,36]. Furthermore, the +4 oxidation state of Ti is unchanged after the formation of WO_3/TiO_2-25 heterojunctions as the energy gap between the peaks at 459.1 and 464.8 eV remains 5.7 eV. The W 4f XPS spectra of pure WO_3 nanosheets and WO_3/TiO_2-25 heterojunctions are shown in Figure 3b. The two XPS peaks of pure WO_3 nanosheets at 35.7 eV and 37.8 eV are attributed to W $4f_{7/2}$ and W $4f_{5/2}$, respectively. The energy gap between W $4f_{7/2}$ and W $4f_{5/2}$ peaks is 2.1 eV, which suggests that the W element existed in the form of W^{6+} in WO_3 nanosheets [34,36]. For WO_3/TiO_2-25 heterojunctions, the binding energies of W $4f_{7/2}$ and W $4f_{5/2}$ peaks were both shifted to low energy by 0.1 eV, while the energy gap between these two peaks is unchanged, indicating the W^{6+} oxidation state in WO_3/TiO_2-25 heterojunctions [34,36,48], which is in good agreement with the XRD data. The high-resolution O 1s XPS spectrum of the samples is shown in Figure 3c,d. It can be seen that the Ti-O bond peak in TiO_2 nanoribbons is located at 530.0 eV (Figure 3c), while the W-O bond peak in WO_3 nanosheets is centered at 530.5 eV (Figure 3d). For WO_3/TiO_2-25 heterojunctions, the binding energy at 530.4 eV corresponded to the lattice oxygen of Ti^{4+}-O or W^{6+}-O, indicating that W-O and Ti-O shared the orbital O 1s in the W-O-Ti bond [32,43,44]. The peak exhibited a 0.4 eV up-shift from Ti-O bonds (from 530.0 to 530.4 eV) and 0.1 eV down-shift from W-O bonds (from 530.5 to 530.4 eV). The above XPS results show that the binding energy of Ti 2p shifted to high energy, while the binding energy of W 4f and O 1s shifted to low energy after the formation of WO_3/TiO_2-25 heterojunctions, confirming the electron density decrease on TiO_2 and electron density increase on WO_3, respectively [36,49,50]. The electron density change indicates that the photo-generated carriers have been successfully transferred between WO_3 and TiO_2 in the composite, which further proved the formation of WO_3/TiO_2-25 heterojunction structures [34,36].

2.5. Optical Analysis

The UV–vis diffuse reflection spectra of TiO_2, WO_3, and WO_3/TiO_2 heterojunctions were recorded to understand the light absorption property and are shown in Figure 4a. The TiO_2 nanoribbons show strong absorbance in the ultraviolet region, and the optical absorption edge was found to be around 400 nm owing to the large band gap of anatase TiO_2 [21,22]. After the combination of WO_3, the optical absorption edge exhibits a 130 nm red shift compared to pure TiO_2 nanoribbons. Thus, the hybrid WO_3/TiO_2 heterostructures can utilize a larger fraction of the solar spectrum for photocatalytic reactions. In order to quantitatively determine their band gaps, $(\alpha h\nu)^{1/2}$ vs. photon energy ($h\nu$) are generated from the diffuse reflectance spectra (Figure 4b). Therein, α is the Kubelka–Munk function of the diffuse reflectance spectra ($\alpha = (1 - R)^2/2R$, and R is the reflectance). The apparent band gaps of pristine TiO_2 and WO_3 were calculated to be 3.12 eV and 2.26 eV, respectively, while the estimated band gap of WO_3/TiO_2 heterostructures was calculated to be 2.30 eV. The band gap reduction in TiO_2 nanoribbons after WO_3 sheet growth suggests the strong interaction between TiO_2 and WO_3 in WO_3/TiO_2 heterostructures, which can effectively hinder the recombination of e-h+ through the WO_3/TiO_2 heterojunction [27,29,35].

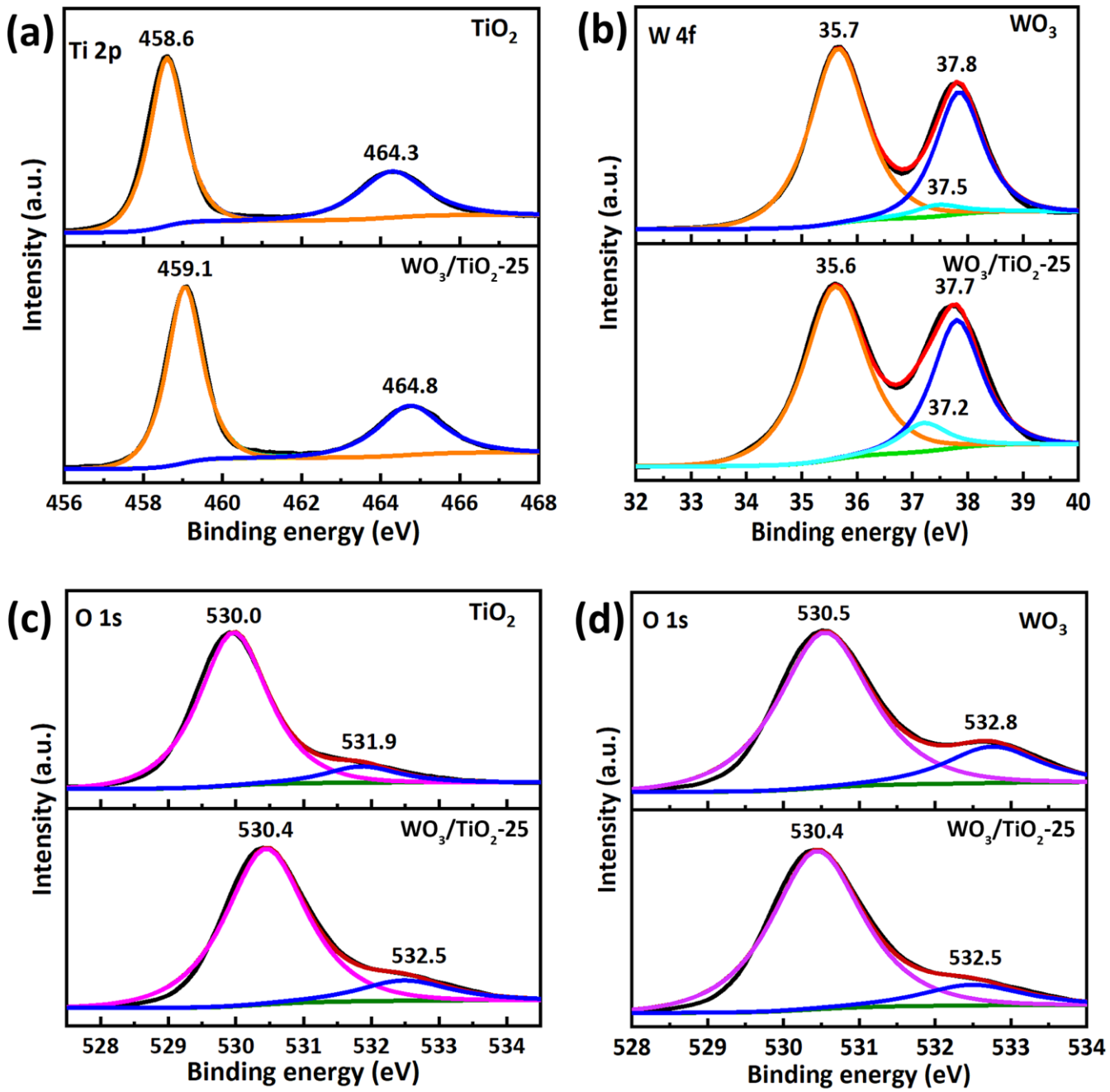

Figure 3. XPS spectra: (**a**) Ti 2p spectra of TiO_2 and WO_3/TiO_2-25 heterojunctions. The orange and blue curves are fitting curves corresponding to the Ti $2p_{1/2}$ and Ti $2p_{3/2}$, respectively. The black line is the raw data. (**b**) W 4f spectra of WO_3 and WO_3/TiO_2-25 heterojunctions. The orange, cyan, blue and green curves are fitting curves corresponding to the W $4f_{7/2}$ and W $4f_{5/2}$, respectively. The black represent the raw data and the red line is the fitting line. (**c**) O 1s spectra of TiO_2 and WO_3/TiO_2-25 heterojunctions. The magenta, blue and olive curves are fitting curves corresponding to the Ti-O bond. The black represent the raw data and the red line is the fitting line. (**d**) O 1s spectra of WO_3 and WO_3/TiO_2-25 heterojunctions. The magenta, blue and olive curves are fitting curves corresponding to the W-O bond. The black represent the raw data and the red line is the fitting line.

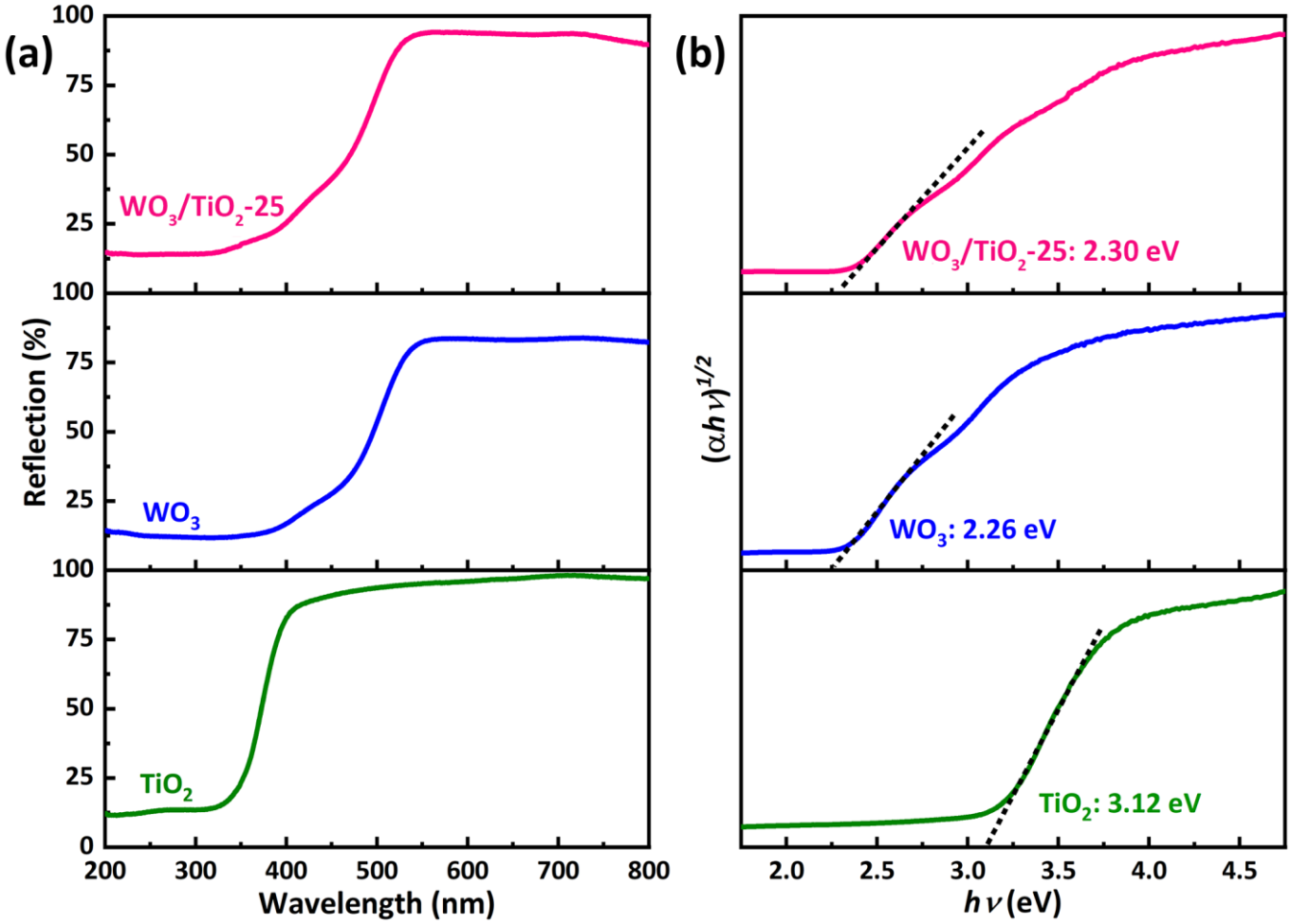

Figure 4. (**a**) Diffuse reflectance spectra for the TiO_2 nanoribbons, WO_3 nanosheets, and WO_3/TiO_2-25 heterojunction. (**b**) Plot of $(\alpha h\nu)^{1/2}$ as a function of photon energy ($h\nu$).

2.6. Photoluminescence Analysis

Photoluminescence measurements were further undertaken to unveil the charge recombination behavior of TiO_2 and WO_3/TiO_2-25 heterostructures. It is widely known that fluorescence emission signals are derived mainly from the recombination of photo-generated electron–hole pairs, and a lower fluorescence intensity signifies a higher photocatalytic efficiency [12,31,43]. Figure 5a shows the fluorescence spectra of TiO_2 and WO_3/TiO_2-25 heterostructures in the wavelength range of 475–725 nm. It can be seen clearly that the emission peaks of TiO_2 and WO_3/TiO_2-25 heterostructures are in similar shapes, and the fluorescence emission intensity of TiO_2 shows an obvious reduction after modification with WO_3 nanosheets, indicating that growth of WO_3 nanosheets on TiO_2 nanoribbons can effectively suppress recombination of electron–hole pairs and increase the lifetime of the charge carriers, which provides solid basis for photocatalytic activity improvement. In order to further confirm the enhanced photo-generated electron–hole separation efficiency, photocurrent responses of all samples have been recorded and shown in Figure S4. The photocurrent of all the WO_3/TiO_2 composite samples is significantly higher than that of the pure TiO_2 and WO_3, further confirming the higher charge separation induced by WO_3 nanosheet growth, which is consistent with photoluminescence spectra. It is worth noting that WO_3/TiO_2-25 exhibits the highest photocurrent density of 7.9 $\mu A \cdot cm^{-2}$, which is roughly 7.1, 6.6 times higher than that of pure TiO_2 nanowires and pure WO_3 nanosheets. The best photocurrent response manifests that the WO_3/TiO_2-25

heterostructure composite possesses the highest photoelectrons–holes transfer efficiency and thus should be a promising candidate as a high-performance photocatalyst.

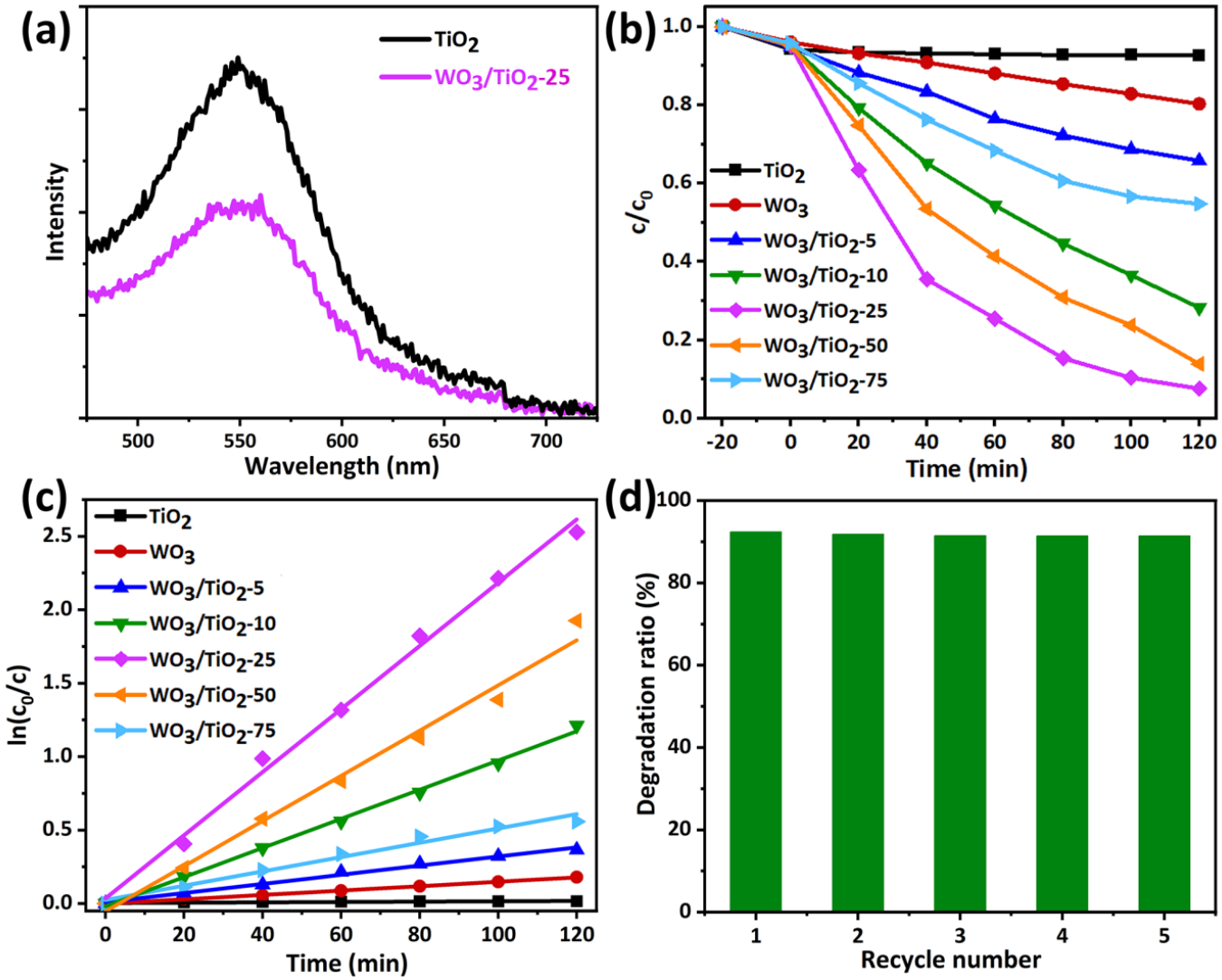

Figure 5. (**a**) Fluorescence spectrum of TiO_2 nanoribbons and WO_3/TiO_2-25 heterojunction. (**b**) Photocatalytic degradation of RhB over various photocatalysts under sunlight irradiation, where C_0 is the initial concentration of the pollutant, and C is the concentration of the pollutant at irradiation time t. (**c**) First-order reaction kinetic curves for the RhB degradation reaction over various photocatalysts. (**d**) Curve of the degradation ratio of RhB versus reuse times of WO_3/TiO_2-25.

2.7. Photocatalytic Performance

UV–vis diffuse reflection, photoluminescence, and photocurrent measurements demonstrate that construction of 2D/1D heterojunctions through vertical growth WO_3 nanosheets on TiO_2 nanoribbons not only broaden the light utilization region but also effectively suppresses electron–hole pair recombination; thus, theoretically, WO_3/TiO_2 heterostructures should possess higher photocatalytic activity than pure TiO_2 and WO_3 [11,12,31]. Figure 5b shows the photocatalytic degradation behavior of RhB over various photocatalysts under visible light irradiation. In the dark condition, all the samples exhibit similar RhB removal efficiency, owing to the similar BET surface area (Figure S3). All five kinds of WO_3/TiO_2 heterostructures prepared under different precursor concentrations show higher photocatalytic activity than pure WO_3 nanosheets and TiO_2 nanoribbons. Of the five heterojunctions, the WO_3/TiO_2-25 system shows the highest photocatalytic activity, which can remove 92.8% of

RhB pollutants in 120 min. The photocatalytic degradation ration of RhB over WO_3/TiO_2-50 and WO_3/TiO_2-10 heterojunctions is 86.3% and 71.7%, respectively, indicating that too much higher and lower growth density of WO_3 nanosheets causes photocatalytic activity decrease. The reason is that over-dense WO_3 nanosheets result in lower exposure of junctions, while sparse growth density leads to few junctions. Figure 5c shows the first-order reaction kinetic curves for the RhB degradation reaction over various photocatalysts. It can be seen that the slope of WO_3/TiO_2 heterostructures is bigger than that of pure WO_3 nanosheets and TiO_2 nanoribbons, suggesting the enhanced photocatalytic rate constant after growth of WO_3 nanosheets on TiO_2 nanoribbons. The enhanced photocatalytic activity of the WO_3/TiO_2 heterostructures is attributed to the synergetic effects of the improved visible light utilization and enhanced electron–hole separation, which have been proven by UV–vis diffuse reflection and photoluminescence spectra. Over five consecutive cycles, there was no notable change for the apparent photocatalytic degradation ratio, indicating the excellent durability of WO_3/TiO_2 heterostructures (Figure 5d).

The effect of WO_3/TiO_2-25 catalyst loading on the photocatalytic degradation ratio of RhB is shown in Figure 6a. The photodegradation ratio increased with the increase in catalyst loading in the range of 5–20 mg and reached a maximum when 20 mg of the catalyst was used. Further increase in catalyst loading from 20 mg to 40 mg led to a decline in the photodegradation ratio from 92.8% to 82.6%. The observation can be explained as follows. Increasing catalyst loading from 5 mg to 20 mg would provide more active photodegradation sites, thus leading to an enhancement of the degradation ratio. When the catalyst was increased to 40 mg, the photodegradation reaction system became thick colloid, reducing the light penetration depth, which means only the catalysts in the solution surface layer can be photo activated as degradation sites, while the catalyst in the solution bottom layer make little contribution to RhB photodegradation, thus resulting in a decline in the degradation ratio [51]. Another reason might be due to catalyst aggregation resulting from high catalyst concentration, which would lead to a decrease in total surface area available for degradation, reduction in site density for surface holes and electrons, and an increase in the diffusion path length [51].

In order to reveal the photocatalytic mechanism, several trapping agents, including ascorbic acid (AC), ammonium oxalate (AO), isopropanol (IPA), and hydrogen peroxide (H_2O_2), were applied as scavengers for probing the active radicals in photocatalytic degradation. The scavengers AC, AO, IPA, and H_2O_2 functioned as trapping agents for superoxide anions (O_2^-), holes (h^+), hydroxyl radicals (OH), as well as electrons (e^-), respectively [52]. As shown in Figure 6b, various sacrificial agents have a great impact on the RhB degradation efficiency. After adding AO, AC, and IPA, the RhB photocatalytic degradation efficiency decreased obviously compared with the blank. The photodegradation ratios of RhB corresponding to AC, AO, and IPA were 40.2%, 20.7%, and 32.2%, respectively, indicating that h^+ and OH constituted the major active species for RhB photodegradation [52]. The photodegradation ratio of RhB reached nearly 100% in the presence of H_2O_2. The addition of H_2O_2 resulted in the consumption of e^- in the conduction band (CB) and the enhancement of photoinduced e^-/h^+ pair separation. Furthermore, H_2O_2 was reduced by e^- to generate OH, as indicated by $H_2O_2 + e^- \rightarrow OH + OH^-$ [53]. The generation of extra ·OH further promoted photocatalytic degradation. Therefore, active species detection reveals that photoinduced h^+ and ·OH were the main active species in the RhB photodegradation process.

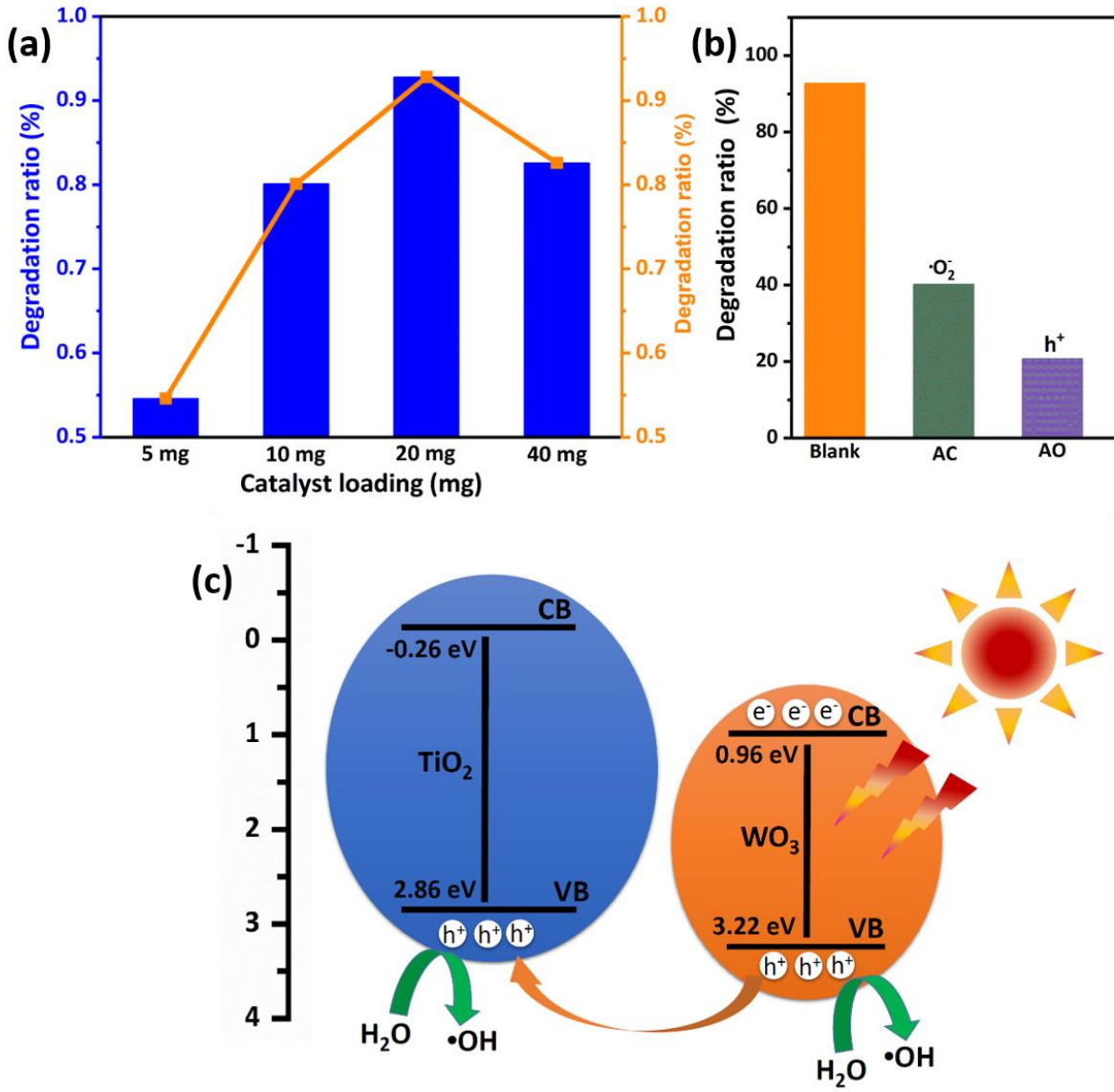

Figure 6. (**a**) The effect of WO_3/TiO_2-25 catalyst loading on RhB photodegradation ratio. (**b**) Trapping test for active species during RhB photodegradation with the WO_3/TiO_2-25 photocatalyst. (**c**) Proposed photocatalytic mechanism of WO_3/TiO_2 photocatalyst.

The conduction band (CB) and the valence band (VB) edge level potentials of TiO_2 and WO_3 were measured by applying the following formula [54]: $E_{VB} = X - E_c + 0.5E_g$, $E_{CB} = E_{VB} - E_g$. Where E_{VB} is the VB edge level potential and E_{CB} is the CB edge level potential, and X is the absolute electronegativity of the semiconductor material (electronegativity of TiO_2 and WO_3 is 5.8 eV and 6.59 eV, respectively) [54]. E_c is the energy of free electrons (4.5 eV vs. NHE), and E_g is the band gap of TiO_2 and WO_3. The CB and VB edge level potentials of TiO_2 were determined as −0.26 eV and 2.86 eV, respectively, while the CB and VB edge level potentials of WO_3 were calculated to be 0.96 eV and 3.22 eV, respectively. The photocatalytic degradation mechanism of the WO_3/TiO_2 heterojunctions is schematically demonstrated in Figure 6c. When WO_3/TiO_2 heterojunction photocatalysts are exposed to visible light irradiation, the photo-generated electrons in the WO_3 valence band will be excited to the conduction band, generating holes in the valence band. However, it cannot occur for TiO_2 due to the band gap energy of TiO_2 (3.12 eV) being higher than

the visible photon energy. The valence band of WO_3 is higher than that of TiO_2 (3.22 eV vs. 2.86 eV), so the photo-generated holes can be easily transferred to the valence band of TiO_2 through the 2D/1D junction interface [31–36]. The photo-generated electrons on the WO_3 conduction band cannot react with O_2 to produce $\bullet O_2^-$ radicals because the conduction edge potential of WO_3 was higher than the redox potential of O_2 to $\bullet O_2^-$ (0.96 eV vs. −0.33 eV). Thus, the radicals of $\bullet O_2^-$ can hardly participate in the photodegradation reaction, which is in good agreement with the scavenger experiment results. Furthermore, photo-generated holes (h^+) can react with adsorbed H_2O or OH^- to generate •OH radicals, which are the main active species for organic pollutant photo-degradation confirmed by the scavenger experiment. The above results showed TiO_2 acted as a photo-generated hole acceptor in the heterojunction, effectively reducing the recombination of photo-generated carriers and enhancing photocatalytic performance, and h^+ and •OH are responsible for the photodegradation of RhB.

3. Materials and Methods

3.1. Preparation of WO_3/TiO_2

TiO_2 nanoribbons were synthesized according to our previous report [55,56]. Then, WO_3 nanosheets were vertically grown on TiO_2 nanoribbons using a hydrothermal process. Typically, 0.1 g of TiO_2 nanoribbons were dispersed in 30 mL of distilled water dissolved by 0.25 g of $Na_2WO_4 \bullet 2H_2O$ (25 mM), 2 mL of 3 mol/L HCl aqueous solution, and 0.3 g of citric acid. Then, the resulting suspension was transferred into a 50 mL Teflon-lined stainless steel autoclave and kept at 120 °C for 24 h. After the hydrothermal reaction was completed, the resulting products were collected by centrifugation, washed several times with deionized water, and dried at 60 °C overnight. For comparison, WO_3/TiO_2 composites with different ratios were prepared in a similar manner. The samples were denoted as WO_3/TiO_2-5, WO_3/TiO_2-10, WO_3/TiO_2-25, and WO_3/TiO_2-50, WO_3/TiO_2-75 in which the number represents the concentration of $Na_2WO_4 \cdot 2H_2O$.

3.2. Material Characterization

The morphology and structure of the photocatalysts were examined by a HITACHlS-4800 field emission scanning electron microscope (SEM, Hitachi, Tokyo, Japan). Transmission electron microscope (TEM, Thermo Fisher Scientific, Waltham, MA, USA) and high-resolution TEM (HRTEM, Thermo Fisher Scientific, Waltham, MA, USA) images were taken with an FEI Tecnai G20 electron microscope. For TEM samples, the photocatalyst was dispersed in ethanol using ultrasonic treatment and the TEM samples were prepared by depositing a drop of diluted suspension on a carbon-coated copper grid. UV-vis-near-infrared (NIR, Agilent, Polo Alto, CA, USA) reflection spectra were recorded on an Agilent Australia Carry-5000 spectrophotometer. The UV–Visible absorption spectra were recorded on a Shimadzu UV-2550 spectrophotometer. The X-ray photoelectron spectroscopy (XPS, Thermo Fisher Scientific, Waltham, MA, USA) analysis was carried out on an Escalab 250Xi spectrometer with monochromatic Al Kα radiation (hν = 1486.7 eV). Phase identification of the photocatalysts was measured by a Shimadzu powder difractometer with Cu-Kα radiation. The solid-state fluorescence spectra were characterized using a FLS980 fluorescence spectrophotometer.

3.3. Photodegradation and Photocurrent Test

Rhodamine B (RhB) solution with a concentration of 9 mg/L was used as the model waste water. An amount of 20 mg of samples were dispersed in 100 mL of RhB solution. The solution was kept in the dark for 20 min and then exposed to visible light irradiation. A 500 W halogen lamp was used as the visible light source, and the average light intensity was 60 mW•cm^{-2}. The distance between the lamp and the solution was 10 cm. During the measurement process, a certain amount of the solution was sampled at certain time

intervals and centrifuged (8000 rpm, 3 min) to remove the photocatalyst particles. The supernatant was analyzed to measure the concentration of RhB by using a Shimadzu UV-2550 UV–vis spectrometer (peak center: 554 nm). To analyze the photocatalytic degradation mechanism, ascorbic acid (AC), ammonium oxalate (AO), isopropanol (IPA), and hydrogen peroxide (H_2O_2) reagents were selected as scavengers for anions (O_2^-), holes (h^+), hydroxyl radicals (·OH), as well as electrons (e^-), respectively. Next, 5 mg of AC, 5 mg of AO, 0.2 mL of IPA, and 0.2 mL of H_2O_2 were added into the above photodegradation system while keeping other conditions unchanged.

Photocurrent studies were performed on a CHI 660D electrochemical workstation using a three-electrode configuration where ITO electrodes were deposited with the samples as a working electrode, Pt as a counter electrode, and a saturated calomel electrode as reference. The electrolyte was 0.35 M/0.25 M Na_2S-Na_2SO_3 aqueous solution. For the fabrication of the working electrode, 0.25 g of the sample was grinded with 0.06 g polyethylene glycol (PEG, molecular weight: 20,000) and 0.5 mL ethanol to make a slurry. The slurry was spread onto a 1 cm × 4 cm ITO glass using the doctor blade technique and then allowed to air-dry. A 500 W halogen lamp was used as the visible light source and the average light intensity was 60 mW•cm^{-2}.

4. Conclusions

In conclusion, a novel WO_3/TiO_2 2D/1D heterojunction photocatalyst was constructed via the introduction of TiO_2 nanoribbons into a WO_3 nanosheet growth system. Two-dimensional WO_3 nanosheets were vertically arrayed on the surface of TiO_2 nanoribbons, and the growth density could be easily controlled by adjusting the concentration of the precursors. The UV–vis diffuse reflection result reveals that vertical growth of WO_3 nanosheets on TiO_2 nanoribbons successfully decreases the band gap energy of TiO_2 from 3.12 to 2.30 eV and broadens the photoresponse range from the UV region to the visible light region. Furthermore, the photoluminescence measurement demonstrates that construction of WO_3/TiO_2 heterojunctions significantly reduces electron–hole pair recombination. Consequently, WO_3/TiO_2 heterostructures with different WO_3 nanosheet growth density show higher photocatalytic activity than pure WO_3 nanosheets and TiO_2 nanoribbons. WO_3/TiO_2-25 possesses the highest photocatalytic activity, which can remove 92.8% of RhB pollutants in 120 min and maintain high removal efficiency after five consecutive cycles. The present study demonstrates that the prepared WO_3/TiO_2 2D/1D heterostructures are promising materials for photocatalytic removal of organic pollutants to purify water.

Supplementary Materials: The following supporting information can be downloaded at: https://www.mdpi.com/article/10.3390/catal13030556/s1, Figure S1: SEM images of WO_3/TiO_2 heterostructures prepared under different precursor concentrations: (a) 5 mM, (b) 10 mM, (c) 50 mM, (d) 75 mM. Figure S2: SEM image of pure WO_3 nanosheets. Figure S3: Nitrogen adsorptione-desorption isotherm: (a) TiO_2 nanoribbons; (b) WO_3 nanosheets; (c) WO_3/TiO_2 heterostructures and Figure S4. Photocurrent responses of all samples.

Author Contributions: Conceptualization, L.Z.; methodology, L.Z., L.W., K.X. and H.T.; validation, L.W. and H.T.; formal analysis, L.W., K.X. and H.T.; investigation, L.Z.; data curation, L.W., K.X. and L.W.; writing—original draft preparation, L.Z.; writing—review and editing, L.Z. and L.W.; visualization, L.W. and K.X.; supervision, L.Z.; project administration, L.Z.; funding acquisition, L.Z. All authors have read and agreed to the published version of the manuscript.

Funding: This research was funded by Jiaxing City Public Welfare Research Project of China, grant number 2021AY10059 and Innovation Jiaxing Excellent Talents Support Program, grant number 84321005.

Data Availability Statement: The data presented in this study are available on request from the corresponding authors.

Conflicts of Interest: The authors declare no conflict of interest.

References

1. McDonald, R.I.; Green, P.; Balk, D.; Montgomery, M. Urban growth, climate change, and freshwater availability. *Proc. Natl. Acad. Sci. USA* **2011**, *108*, 6312–6317. [CrossRef] [PubMed]
2. Oki, T.; Kanae, S. Global hydrological cycles and world water resources. *Science* **2006**, *313*, 1068–1072. [CrossRef] [PubMed]
3. Vörösmarty, C.J.; McIntyre, P.B.; Gessner, M.O.; Dudgeon, D.; Prusevich, A.; Green, P.; Glidden, S.; Bunn, S.E.; Sullivan, C.A.; Liermann, C.R.; et al. Global threats to human water security and river biodiversity. *Nature* **2010**, *467*, 555–561. [CrossRef] [PubMed]
4. Gadgil, A. Drinking Water in Developing Countries. *Annu. Rev. Energy Environ.* **1998**, *23*, 253–286. [CrossRef]
5. Water Scarcity Threats. Available online: https://www.worldwildlife.org/threats/water-scarcity (accessed on 12 January 2023).
6. Shannon, M.A.; Bohn, P.W.; Elimelech, M.; Georgiadis, J.G.; Mariñas, B.J.; Mayes, A.M. Science and technology for water purification in the coming decades. *Nature* **2008**, *452*, 301–310. [CrossRef]
7. Macedonio, F.; Drioli, E.; Gusev, A.A.; Bardow, A.; Semiatf, R.; Kuriharag, M. Efficient technologies for worldwide clean water supply. *Chem. Eng. Process.* **2012**, *51*, 2–17. [CrossRef]
8. Tee, G.T.; Gok, X.Y.; Yong, W.F. Adsorption of pollutants in wastewater via biosorbents, nanoparticles and magnetic biosorbents: A review. *Environ. Res.* **2022**, *212*, 113248. [CrossRef]
9. Ouachtak, H.; Akhouairi, S.; Haounati, R.; Addi, A.A.; Jada, A.; Taha, M.L.; Douch, J. 3,4-Dihydroxybenzoic acid removal from water by goethite modified natural sand column fixed-bed: Experimental study and mathematical modeling. *Desalin. Water Treat.* **2020**, *194*, 439–449. [CrossRef]
10. Pendergast, M.T.M.; Eric, M.V.; Hoek, E.M.V. A review of water treatment membrane nanotechnologies. *Energy Environ. Sci.* **2011**, *4*, 1946–1971. [CrossRef]
11. Andrew, M.; Davies, R.H.; Worsley, D. Water purification by semiconductor photocatalysis. *Chem. Soc. Rev.* **1993**, *22*, 417–425.
12. Parvulescu, V.I.; Epron, F.; Garcia, H.; Granger, P. Recent progress and prospects in catalytic water treatment. *Chem. Rev.* **2021**, *122*, 2981–3121. [CrossRef] [PubMed]
13. Schneider, J.; Matsuoka, M.; Takeuchi, M.; Zhang, J.; Horiuchi, Y.; Anpo, M.; Bahnemann, D.W. Understanding TiO_2 Photocatalysis: Mechanisms and Materials. *Chem. Rev.* **2014**, *114*, 9919–9986. [CrossRef] [PubMed]
14. Kumar, A.; Choudhary, P.; Kumar, A.; Camargo, P.H.; Krishnan, V. Recent advances in plasmonic photocatalysis based on TiO_2 and noble metal nanoparticles for energy conversion, environmental remediation, and organic synthesis. *Small* **2022**, *18*, 2101638. [CrossRef] [PubMed]
15. Weng, B.; Lu, K.Q.; Tang, Z.C.; Chen, H.M.; Xu, Y.J. Stabilizing ultrasmall Au clusters for enhanced photoredox catalysis. *Nat. Commun.* **2018**, *9*, 1543. [CrossRef] [PubMed]
16. Pan, X.; Chen, W.J.; Cai, H.; Li, H.; Sun, X.J.; Weng, B.; Yi, Z. A redox-active support for the synthesis of Au@SnO_2 core-shell nanostructure and SnO_2 quantum dots with efficient photoactivities. *RSC Adv.* **2020**, *10*, 33955–33961. [CrossRef] [PubMed]
17. Haounati, R.; Alakhras, F.; Ouachtak, H.; Saleh, T.A.; Al-Mazaideh, G.; Alhajri, E.; Jada, A.; Hafid, N.; Addi, A.A. Synthesized of Zeolite@Ag_2O Nanocomposite as Superb Stability Photocatalysis toward Hazardous Rhodamine B Dye from Water. *Arab. J. Sci. Eng.* **2023**, *48*, 169–179. [CrossRef]
18. Nawaz, A.; Goudarzi, S.; Asghari, M.A.; Pichiah, S.; Selopal, G.S.; Rosei, F.; Wang, Z.M.; Zarrin, H. Review of Hybrid 1D/2D Photocatalysts for Light-Harvesting Applications. *ACS Appl. Nano Mater.* **2021**, *4*, 11323–11352. [CrossRef]
19. Hou, H.; Zhang, X. Rational design of 1D/2D heterostructured photocatalyst for energy and environmental applications. *Chem. Eng. J.* **2020**, *395*, 125030. [CrossRef]
20. Fujishima, A.; Honda, K. Electrochemical photolysis of water at a semiconductor electrode. *Nature* **1972**, *238*, 37–38. [CrossRef]
21. Ren, Y.; Dong, Y.; Feng, Y.; Xu, J. Compositing two-dimensional materials with TiO_2 for photocatalysis. *Catalysts* **2018**, *8*, 590. [CrossRef]
22. Guo, Q.; Zhou, C.; Ma, Z.; Yang, X. Fundamentals of TiO_2 photocatalysis: Concepts, mechanisms, and challenges. *Adv. Mater.* **2019**, *31*, 1901997. [CrossRef] [PubMed]
23. Feng, T.; Feng, G.S.; Yan, L. One-dimensional nanostructured TiO_2 for photocatalytic degradation of organic pollutants in wastewater. *Int. J. Photoenergy* **2014**, *2014*, 563879. [CrossRef]
24. Ge, M.; Cao, C.; Huang, J. A review of one-dimensional TiO_2 nanostructured materials for environmental and energy applications. *J. Mater. Chem. A* **2016**, *4*, 6772–6801. [CrossRef]
25. Szilágyi, I.M.; Fórizs, B.; Rosseler, O.; Szegedi, Á.; Németh, P.; Király, P.; Tárkányi, G.; Vajna, B.; Katalin, V.-J.; László, K. WO_3 photocatalysts: Influence of structure and composition. *J. Catal.* **2012**, *294*, 119–127. [CrossRef]
26. Dutta, V.; Sharma, S.; Raizada, P.; Thakurb, V.K.; Parvaz, K.A.A.; Sainie, V.; Asiri, A.M.; Singha, P. An overview on WO_3 based photocatalyst for environmental remediation. *J. Environ. Chem. Eng.* **2021**, *9*, 105018. [CrossRef]
27. Wang, F.; Valentin, C.D.; Pacchioni, G. Rational band gap engineering of WO_3 photocatalyst for visible light water splitting. *Mater. Sci. ChemCatChem.* **2012**, *4*, 476–478. [CrossRef]
28. Liu, D.; Zhang, S.; Wang, J.; Peng, T.; Li, R. Direct Z-scheme 2D/2D photocatalyst based on ultrathin g-C_3N_4 and WO_3 nanosheets for efficient visible-light-driven H_2 generation. *ACS Appl. Mater. Interfaces* **2019**, *11*, 27913–27923. [CrossRef]

29. Lei, B.; Cui, W.; Chen, P.; Chen, L.; Li, J.; Dong, F. C-doping induced oxygen-vacancy in WO_3 nanosheets for CO_2 activation and photoreduction. *ACS Catal.* **2022**, *12*, 9670–9678. [CrossRef]
30. Liang, Y.; Yang, Y.; Zou, C.; Xu, K.; Luo, X.; Luo, T.; Li, J.; Yang, Q.; Shi, P.; Yuan, C. 2D ultra-thin WO_3 nanosheets with dominant {002} crystal facets for high-performance xylene sensing and methyl orange photocatalytic degradation. *J. Alloy. Compd.* **2019**, *783*, 848–854. [CrossRef]
31. Lai, C.W. WO_3-TiO_2 Nanocomposite and its applications: A review. *Nano Hybrids Compos.* **2018**, *20*, 1–26. [CrossRef]
32. Zhang, L.; Qin, M.; Yu, W.; Zhang, Q.; Xie, H.; Sun, Z.; Shao, Q.; Guo, X.; Hao, L.; Zheng, Y.; et al. Heterostructured TiO_2/WO_3 nanocomposites for photocatalytic degradation of toluene under visible light. *J. Electrochem. Soc.* **2017**, *164*, H1086–H1090. [CrossRef]
33. Liu, Y.; Xie, C.; Li, J.; Zou, T.; Zeng, D. New insights into the relationship between photocatalytic activity and photocurrent of TiO_2/WO_3 nanocomposite. *Appl. Catal. A* **2012**, *433–434*, 81–87. [CrossRef]
34. Prabhu, S.; Cindrella, L.; Kwon, O.J.; Mohanrajubet, K. Photoelectrochemical and photocatalytic activity of TiO_2-WO_3 heterostructures boosted by mutual interaction. *Mater. Sci. Semicond. Process.* **2018**, *88*, 10–19. [CrossRef]
35. Yang, J.; Zhang, X.; Liu, H.; Wang, C.; Liu, S.; Sun, P.; Wang, L.; Liu, Y. Heterostructured TiO_2/WO_3 porous microspheres: Preparation, characterization and photocatalytic properties. *Catal. Today* **2013**, *201*, 195–202. [CrossRef]
36. Wang, Q.; Zhang, W.; Hu, X.; Xua, L.; Chen, G.; Li, X. Hollow spherical WO_3/TiO_2 heterojunction for enhancing photocatalytic performance in visible-light. *J. Water Process. Eng.* **2021**, *40*, 101943. [CrossRef]
37. Zhang, Y.; Xu, M.; Li, H.; Ge, H.; Bian, Z. The enhanced photoreduction of Cr (VI) to Cr (III) using carbon dots coupled TiO_2 mesocrystals. *Appl. Catal. B* **2018**, *226*, 213–219. [CrossRef]
38. Song, Y.Y.; Gao, Z.D.; Wang, J.H.; Xia, X.H.; Lynch, R. Multistage coloring electrochromic device based on TiO_2 nanotube arrays modified with WO_3 nanoparticles. *Adv. Funct. Mater.* **2011**, *21*, 1941–1946. [CrossRef]
39. Paramasivam, I.; Nah, Y.C.; Das, C.; Shrestha, N.K.; Schmuki, P. WO_3/TiO_2 nanotubes with strongly enhanced photocatalytic activity. *Chem. Eur. J.* **2010**, *16*, 8993–8997. [CrossRef]
40. Xu, T.; Wang, Y.; Zhou, X.; Zheng, X.; Xu, Q.; Chen, Z.; Ren, Y.; Yan, B. Fabrication and assembly of two-dimensional $TiO_2/WO_3{\cdot}H_2O$ heterostructures with type II band alignment for enhanced photocatalytic performance. *Appl. Surf. Sci.* **2017**, *403*, 564–571. [CrossRef]
41. Lee, J.Y.; Jo, W.K. Heterojunction-based two-dimensional N-doped TiO_2/WO_3 composite architectures for photocatalytic treatment of hazardous organic vapor. *J. Hazard. Mater.* **2016**, *314*, 22–31. [CrossRef]
42. Liu, J.; Yang, L.; Li, C.; Chen, Y.; Zhang, Z. Optimal monolayer WO_3 nanosheets/TiO_2 heterostructure and its photocatalytic performance under solar light. *Chem. Phys. Lett.* **2022**, *804*, 139861. [CrossRef]
43. Mei, Y.; Su, Y.; Li, Z.; Bai, S.; Yuan, M.; Li, L.; Yan, Z.; Wu, J.; Zhu, L.W. BiOBr nanoplates@TiO_2 nanowires/carbon fiber cloth as a functional water transport network for continuous flow water purification. *Dalton Trans.* **2017**, *46*, 347–354. [CrossRef] [PubMed]
44. Chen, J.Z.; Ko, W.Y.; Yen, Y.C.; Chen, P.H.; Lin, K.J. Hydrothermally processed TiO_2 nanowire electrodes with antireflective and electrochromic properties. *ACS Nano* **2012**, *6*, 6633–6639. [CrossRef] [PubMed]
45. Li, F.; Li, C.; Zhu, L.; Guo, W.; Shen, L.; Wen, S.; Ruan, S. Enhanced toluene sensing performance of gold-functionalized $WO_3{\cdot}H_2O$ nanosheets. *Sens. Actuators B Chem.* **2016**, *223*, 761–767. [CrossRef]
46. Liu, W.; Du, T.; Ru, Q.; Zuo, S.; Cai, Y.; Yao, C. Preparation of graphene/WO_3/TiO_2 composite and its photocathodic protection performance for 304 stainless steel. *Mater. Res. Bull.* **2018**, *102*, 399–405. [CrossRef]
47. Idriss, H.; Barteau, M.A. Characterization of TiO_2 surfaces active for novel organic syntheses. *Catal. Lett.* **1994**, *26*, 123–139. [CrossRef]
48. Chen, S.; Chen, L.; Gao, S.; Ca, G. The preparation of coupled WO_3/TiO_2 photocatalyst by ball milling. *Powder Technol.* **2005**, *160*, 198–202.
49. Li, S.; Wang, P.; Wang, R.; Liu, Y.; Jing, R.; Zi, Z.; Meng, L.; Liu, Y.; Zhang, Q. One-step co-precipitation method to construct black phosphorus nanosheets/ZnO nanohybrid for enhanced visible light photocatalytic activity. *Appl. Surf. Sci.* **2019**, *497*, 143682. [CrossRef]
50. Zhang, Z.; Liu, K.; Feng, Z.; Bao, Y.; Dong, B. Hierarchical sheet-on-sheet $ZnIn_2S_4$/g-C_3N_4 heterostructure with highly efficient photocatalytic H_2 production based on photoinduced interfacial charge transfer. *Sci. Rep.* **2016**, *6*, 19221. [CrossRef]
51. Paul, D.R.; Sharma, R.; Nehra, S.P.; Sharma, A. Effect of calcination temperature, pH and catalyst loading on photodegradation efficiency of urea derived graphitic carbon nitride towards methylene blue dye solution. *RSC Adv.* **2019**, *9*, 15381–15391. [CrossRef]
52. Gao, J.; Hu, J.; Wang, Y.; Zheng, L.; He, G.; Deng, J.; Liu, M.; Li, Y.; Liu, Y.; Zhou, H. Fabrication of Z-Scheme $TiO_2/SnS_2/MoS_2$ ternary heterojunction arrays for enhanced photocatalytic and photoelectrochemical performance under visible light. *J. Solid State Chem.* **2022**, *307*, 122737. [CrossRef]
53. Zhu, B.; Xia, P.; Li, Y.; Ho, W.; Yu, J. Fabrication and photocatalytic activity enhanced mechanism of direct Z-scheme g-C_3N_4/Ag_2WO_4 photocatalyst. *Appl. Surf. Sci.* **2017**, *391*, 175–183. [CrossRef]

54. Vembuli, T.; Thiripuranthagan, S.; Sureshkumar, T.; Erusappan, E.; Kumaravel, S.; Kasinathan, M.; Sivakumar, A. Degradation of Harmful Organics Using Visible Light Driven N-TiO_2/rGO Nanocomposite. *J. Nanosci. Nanotechnol.* **2021**, *21*, 3081–3091. [CrossRef] [PubMed]
55. Zhu, L.; Gu, L.; Zhou, Y.; Cao, S.; Cao, X. Direct production of a free-standing titanate and titania nanofiber membrane with selective permeability and cleaning performance. *J. Mater. Chem.* **2011**, *21*, 12503–12510. [CrossRef]
56. Zhou, Y.; Zhu, L.; Gu, L.; Cao, S.; Wang, L.; Cao, X. Guided growth and alignment of millimetre-long titanate nanofibers in solution. *J. Mater. Chem.* **2012**, *22*, 16890–16896. [CrossRef]